JOURNAL OF AIRCRAFT
Vol. 43, No. 6, November–December 2006

Data Analysis of Phoenix Reusable Launch Vehicle Demonstrator Flight Test

Ravindra Jategaonkar*
DLR, German Aerospace Center, 38108 Braunschweig, Germany
Roland Behr†
European Aeronautic Defence and Space Company, Space Transportation, 81663 Munich, Germany
Wilhelm Gockel‡
European Aeronautic Defence and Space Company, Space Transportation, 28361 Bremen, Germany
and
Christoph Zorn§
DLR, German Aerospace Center, 38108 Braunschweig, Germany

DOI: 10.2514/1.19602

The Phoenix vehicle was designed to flight demonstrate the automatic and unpowered horizontal landing of a representative, winged reusable launch vehicle. The shape of the test vehicle was derived from the suborbital reusable launch vehicle concept Hopper. Three automatic landing tests were completed successfully in May 2004. Methods of system identification were applied to the flight data to evaluate the performance and to improve the design models and databases for future applications. A specific emphasis was placed on the evaluation of the onboard navigation system, air data sensor, aerodynamic model, landing gear effects and ground-roll characteristics. This paper gives a brief overview of the Phoenix mission and elaborates on the flight data analysis and of the preceding wind-tunnel campaigns, to allow a comparison of results from different approaches.

I. Introduction

PHOENIX flight-test vehicle was developed and tested within the framework of the German Advanced Systems & Technologies for reusable launch vehicle (RLV) Application (ASTRA) Program, which is a precursor to the European Future Launcher Preparatory Program (FLPP) [1,2]. The primary objective of the Phoenix project was to demonstrate the unpowered automatic landing of a representative RLV configuration. The secondary goal was to generate flight validated database incorporating representative models of such vehicles and its systems as well as development tools for future applications. The project had its kickoff in April 2001 and reached its climax with the flight-test campaign in May 2004 [3,4].

RLV configurations compromise between partly contradicting demands derived from various system optimization aspects as well as the different flight phases covering ascent, orbital phase, reentry, hypersonic flight, and landing. The resultant vehicle typically is characterized by a compact shape with small span wings and stabilizers, and a rearward center of gravity (CG) location. Such properties challenge an automatic horizontal landing on a runway, which in addition must be performed without engine thrust. The important characteristics and their impact on the landing phase can be summarized as follows: 1) low L/D (5.5 for Phoenix) causing steep approach path, 2) low achievable lift coefficient (CL) causing high landing velocity (71 m/s for Phoenix), 3) small span causing high roll sensitivity, and 4) aft CG position causing a statically unstable configuration (time to double amplitude <0.5 s for Phoenix).

The test vehicle shape was derived from the suborbital RLV concept Hopper, one of the three RLV concept families currently studied in Europe. Besides guidance, navigation, and control (GNC) and avionics systems for autonomous approach and landing, the vehicle is equipped with flight-test instrumentation to measure local aerodynamic flow and structural stress.

Two other projects, namely, X-40A and ALFLEX, have also demonstrated successful free-flight and automatic landing experiments in the past [5,6]. Compared to Phoenix, ALFLEX vehicle was smaller and lighter, with not so high wing loading resulting in lower landing speed and did not have extendable landing gear system. Moreover, it was equipped with ground-supported microwave based landing system [6]. Phoenix configuration is more demanding and incorporates fully autonomous DGPS based system, which is more advanced.

Three free flights, launched from a carrier helicopter at 2.4 km altitude, were successfully completed in May 2004. The data obtained from these tests established the source for the verification of the vehicle model. In particular, methods of system identification were applied to upgrade the aerodynamic and the wheel-ground contact and ground-roll model.

II. Landing Flight Test

The nominal reference mission involves a helicopter towing to establish the initial conditions for the flight test, and the subsequent free-flight phase of the Phoenix, which is fully controlled by the autopilot. The helicopter lifts the vehicle to over 2400 m above runway level and drops the Phoenix in steady horizontal forward flight at some 80 kn speed. The drop positions are certain distance forward and above of the nominal final approach path of a RLV (see Fig. 1). Upon release from the carrier device the vehicle goes through the following phases of its autonomous free flight [3]:

1) Acquisition Phase: Release of the Phoenix from the helicopter occurs at some 40 m/s equivalent airspeed, which is below the

Presented as Paper 6129 at the AIAA Atmospheric Flight Mechanics, San Francisco, CA, 15–18 August 2002; received 22 August 2005; accepted for publication 12 July 2006.

*Senior Scientist, DLR Institute of Flight Systems, Lilienthalplatz 7. Associate Fellow AIAA.
†R&D Engineer, Department TP 21.
‡Senior Engineer, Department TO 73.
§Scientist, DLR Institute of Flight Systems, Lilienthalplatz 7.

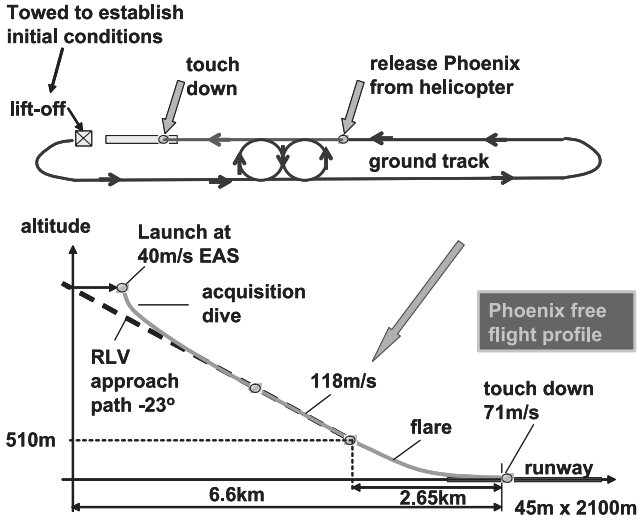

Fig. 1 Phoenix reference mission.

steady-state downward glide speed. Therefore the vehicle enters a controlled dive upon release to gather speed.

2) Approach Phase: After reaching a certain speed threshold ensuring an aerodynamic force of the size of the weight force, the guidance is activated to steer the vehicle to the desired nominal approach path and to maintain steady-state approach conditions, which are representative for RLV.

3) Flare Phase: At a certain height above ground the vehicle starts to flare in order to gradually reduce the sink speed to the desired touchdown value in the remaining flight phase. A load factor of about 1.5 is encountered in the first part of the flare with gradual fading to the end. The vehicle decelerates as the glide slope is no longer sufficient to allow for a balance of the drag by the weight force. Landing gear deployment is commanded when passing 40 m height above ground.

4) Alignment Phase: Few seconds before touchdown, lateral tracking errors are no longer rejected by banking the lift force, but wings are commanded level to accommodate to the desired touchdown attitude.

5) Derotation Phase: After main gear touchdown the vehicle performs a controlled pitch-down motion to limit the loads at nose gear touchdown. Any possible decrab due to crosswinds is also rejected by aligning the vehicle with the runway before nose gear ground contact.

6) Rollout Phase: Once all wheels have ground contact the deceleration on ground begins. It is supported by fully deployed speedbrakes and main gear wheel brakes. Lateral-directional control on ground is achieved by rudder deflection and nose gear steering.

The basis for the data analysis, comprising data compatibility check, aerodynamic model validation, and model update using system identification, is the flight data collected from the three free flights.

III. Data Compatibility and Navigation Filter Check

The aim of data compatibility check is to ensure that the flight measurements are consistent and error free before estimation of aerodynamic parameters. This is possible through a procedure called "flight-path reconstruction" based on the well-defined kinematic equations of aircraft motion. Using redundancies in the measured variables to reveal possible calibration and other sources of errors, correction terms are identified and applied to the data.

The airspeed, angle of attack, and angle of sideslip, the vital feedback variables for the flight control, are obtained from the pressure measurements of the five-hole probe mounted on a nose boom applying algorithms and parameters extracted from calibration tests performed during the wind-tunnel campaign. A linear calibration factor for angle of attack yields error between the probe measured and nominal angle shown in Fig. 2. The nonlinear nature of

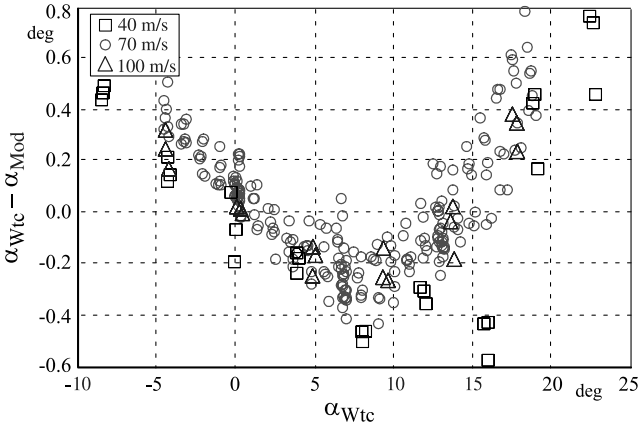

Fig. 2 Errors in linear calibration of angle of attack.

the error necessitated nonlinear calibration factor to achieve the desired accuracy of better than 0.5 deg throughout the range; moreover the angle of attack was also found to be a function of the sideslip angle. Correction factors were also necessary for the angle of sideslip. Likewise, measured dynamic pressure had to be corrected for errors in the static pressure probe [7].

In this project, the flight-path reconstruction has also another important objective. The results have been used as an independent navigation solution to check the accuracy of the navigation filter and the plausibility of selected sensor signals. This aspect of flight-path reconstruction has been more relevant during the captive flights in preparation for the free-flight tests. The flight-path reconstruction model consists of two main parts, namely, state integration and observer equations. In a first step the measured accelerations and angular rates are integrated to obtain kinematic states, namely, attitude, velocity, and position of the reference point called computed specific force origin (CSFO). In a second step the states are used to compute corresponding simulated observer signals which should have been observed by the sensors.

The modeled sensor signals are embedded GPS/INS (EGI) attitude and velocity, differential global positioning system (DGPS) velocity and position, laser ranger distance to ground, radar altitude above ground level, navigation filter with accelerations of CG, flight-path speed and azimuth, position of CG in runway frame, and CG altitude above ground level, as well as air data system (ADS) with true air speed and flow angles. The ADS simulation either considers measured wind data or assumes the absence of wind. In the latter case the deviation to the measured ADS signals can be used to estimate the current wind situation.

For all the three free flights investigated at the same time, it was sufficient to estimate a joint set of small biases which is used to correct the accelerations and angular rates as well as a time delay for the DGPS signals. In this examination, the EGI attitude angles, DGPS velocities and global position are chosen to be the relevant output signals which proved to provide a compatible data set. The remaining mismatch of measured and reconstructed EGI attitude angles is up to 0.1 deg which is well within the required accuracy of 0.3 deg. The same is true for DGPS velocities with mismatch smaller than 0.5 m/s (required: 0.8 m/s horizontal) and DGPS position with an accuracy of $5e-7$ rad ($\approx$3 m) for longitude, $2e-7$ rad ($\approx$1.2 m) for latitude. DGPS-altitude mismatch was about 0.5 m for the first two flights, whereas for the third flight it was roughly 3 m. The required accuracy of lateral position which amounts to 10 m is fulfilled. A more detailed description of the sensors, instrumentation, and data recording system is found in [3,4].

IV. Aerodynamic Model Validation and Update

A two-step general approach to verify and update the aerodynamic model is illustrated in Fig. 3. The first step of verification makes a comparison of aerodynamic forces and moments derived from wind-tunnel measurements and results from computational fluid dynamics

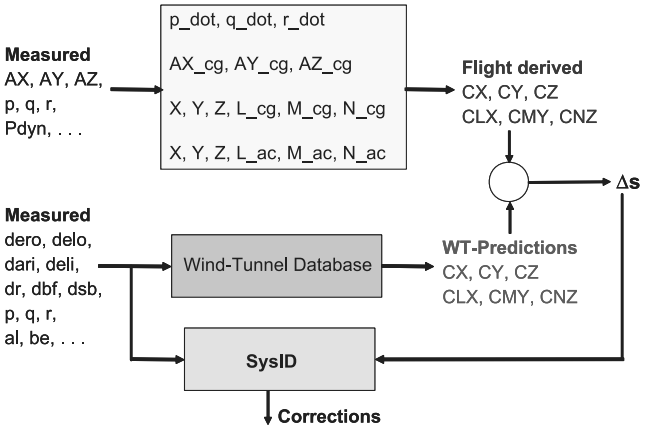

Fig. 3 Schematic of two-step procedure for aerodynamic model verification and update.

with those computed from the flight measured translational accelerations and angular rates. In the second step, correction terms are identified applying a regression approach. In the present case regression analysis is preferred because 1) it allows direct comparison of flight determined force and moment coefficients with the wind-tunnel predictions, 2) the correction terms can be identified as increments or so-called deltas, 3) it is applicable to unstable configurations, and 4) it accounts for the atmospheric turbulence in the estimation.

A. Flight-Derived Aerodynamic Forces and Moments

The body-fixed accelerations $(a_{x,\mathrm{CG}}, a_{y,\mathrm{CG}}, a_{z,\mathrm{CG}})$ at the CG are computed from the translational accelerations $(a_{x,\mathrm{CSFO}}, a_{y,\mathrm{CSFO}}, a_{z,\mathrm{CSFO}})$ measured at CSFO, the reference point of the EGI, through the following transformation:

$$\begin{aligned} a_{x,\mathrm{CG}} &= a_{x,\mathrm{CSFO}} + x_{\mathrm{CSFO\_CG}}(q^2+r^2) - y_{\mathrm{CSFO\_CG}}(pq-\dot{r}) \\ &\quad - z_{\mathrm{CSFO\_CG}}(pr+\dot{q}) \\ a_{y,\mathrm{CG}} &= a_{y,\mathrm{CSFO}} - x_{\mathrm{CSFO\_CG}}(pq+\dot{r}) + y_{\mathrm{CSFO\_CG}}(p^2+r^2) \\ &\quad - z^2_{\mathrm{CSFO\_CG}}(qr-\dot{p}) \\ a_{z,\mathrm{CG}} &= a_{z,\mathrm{CSFO}} - x_{\mathrm{CSFO\_CG}}(pr-\dot{q}) - y_{\mathrm{CSFO\_CG}}(qr+\dot{p}) \\ &\quad + z_{\mathrm{CSFO\_CG}}(p^2+q^2) \end{aligned} \tag{1}$$

where (p, q, r) are the measured angular rates, $(\dot{p}, \dot{q}, \dot{r})$ the angular accelerations obtained by numerical differentiation of measured angular rates, and $x_{\mathrm{CSFO\_CG}}, y_{\mathrm{CSFO\_CG}}, z_{\mathrm{CSFO\_CG}}$ the distances of the CSFO reference point to the CG along the three coordinate axes.

Having obtained the accelerations at the CG, the total forces (X, Y, Z) along the three axes and the three aerodynamic force coefficients (CX, CY, CZ) are then obtained as

$$\begin{aligned} X &= ma_{x,\mathrm{CG}} \qquad Y = ma_{y,\mathrm{CG}} \\ Z &= ma_{z,\mathrm{CG}} \quad \text{and} \quad CX = X/(\bar{q}S_{\mathrm{ref}}) \qquad CY = Y/(\bar{q}S_{\mathrm{ref}}) \\ &\qquad\qquad CZ = Z/(\bar{q}S_{\mathrm{ref}}) \end{aligned} \tag{2}$$

where m is the aircraft mass (1198 kg), $\bar{q}$ is the dynamic pressure, and $S_{\mathrm{ref}}(=10.3\ \mathrm{m}^2)$ is the reference area.

The moments (L, M, N) at the CG and (LX, MY, NZ) at the aerodynamic reference point, aerodynamic center (AC), are computed, respectively, as

$$\begin{aligned} L &= I_X\dot{p} - I_{XZ}\dot{r} - I_{XZ}pq - (I_Y - I_Z)qr \\ M &= I_Y\dot{q} + I_{XZ}(p^2 - r^2) - (I_Z - I_X)pr \\ \mathrm{N} &= I_Z\dot{r} - I_{XZ}\dot{p} + I_{XZ}qr - (I_X - I_Y)pq \quad \text{and} \\ LX &= L - y_{\mathrm{AC\_CG}}Z + z_{\mathrm{AC\_CG}}Y \\ MY &= M - z_{\mathrm{AC\_CG}}\mathrm{X} + x_{\mathrm{AC\_CG}}Z \\ NZ &= N - x_{\mathrm{AC\_CG}}Y + y_{\mathrm{AC\_CG}}X \end{aligned} \tag{3}$$

where (X, Y, Z) are given by Eq. (2), and $(x_{\mathrm{AC\_CG}}, y_{\mathrm{AC\_CG}}, z_{\mathrm{AC\_CG}})$ is the distance from AC to CG. The aerodynamic moment coefficients are now obtained as

$$\begin{aligned} CLX = LX/(q_{\mathrm{dyn}}S_{\mathrm{ref}}B_{\mathrm{ref}}) \qquad CMY = MY/(q_{\mathrm{dyn}}S_{\mathrm{ref}}L_{\mathrm{ref}}) \\ CNZ = NZ(q_{\mathrm{dyn}}S_{\mathrm{ref}}B_{\mathrm{ref}}) \end{aligned} \tag{4}$$

where $L_{\mathrm{ref}}(=6\ \mathrm{m})$ and $B_{\mathrm{ref}}(=3.48\ \mathrm{m})$ are the reference lengths for the longitudinal and lateral-directional modes, respectively. This data preprocessing step, depicted in the upper part of Fig. 3, yields flight-derived $(CX, CY, CZ, CLX, CMY, CNZ)$.

B. Corrections of Flight Measurements

The computation of CX, CY, CZ, CLX, CMY, and CNZ requires measurements of three accelerations $(a_{x,\mathrm{CSFO}}, a_{y,\mathrm{CSFO}}, a_{z,\mathrm{CSFO}})$, the three angular rates (p, q, r), and the dynamic pressure $\bar{q}$. Any errors in the measurements of these variables will directly affect the derived force and moment coefficients. Hence, it is necessary to correct these measurements for possible errors before the aforementioned computations. Likewise the identification of updates, if necessary, would require corrected angle of attack and angle of sideslip.

Based on the ADS calibration results, the dynamic pressure $\bar{q}$ is corrected as follows [7]:

$$\bar{q} = 1.101907\bar{q}_m \tag{5}$$

where $\bar{q}_m$ is the dynamic pressure recorded as the difference between the total and static pressures measured by the five-hole probe. Basically, this correction factor was necessitated by erroneous measurement of the static pressure. Similar corrections have also been reported in other investigations [8].

To reverify the plausibility of the correction in Eq. (5), measured static pressure from the five-hole probe is compared with that measured by a balloon before the flight test. The balloon measurement was roughly 1–2 h before the actual flight test, as such the comparison is not precise; nevertheless, it does help to correlate the results which were obtained through ADS calibration. Figure 4 shows the difference between the static pressures measured by five-hole probe and by balloon, plotted as a function of dynamic pressure. It is evident from Fig. 4 that the static pressure measured by the five-hole probe is incorrect and the error is roughly linear. Based on the results of flight-path reconstruction of the three free flights, the measured accelerations and angular rates, angle of attack, and angle of sideslip were also corrected.

C. Preflight ADB

The prediction model providing aerodynamic forces and moments acting on the airframe was derived from wind-tunnel measurements and some theoretical models [9]. This preflight ADB database predicts the aerodynamic forces and moments in body-fixed axes system referred to an aerodynamic reference point AC. Defining the application rules for the three force and three moment coefficients $(CX, CY, CZ, CLX, CMY, CNZ)$ is not within the scope of this paper, but as a typical example, the vertical force coefficient is given by [9,10]

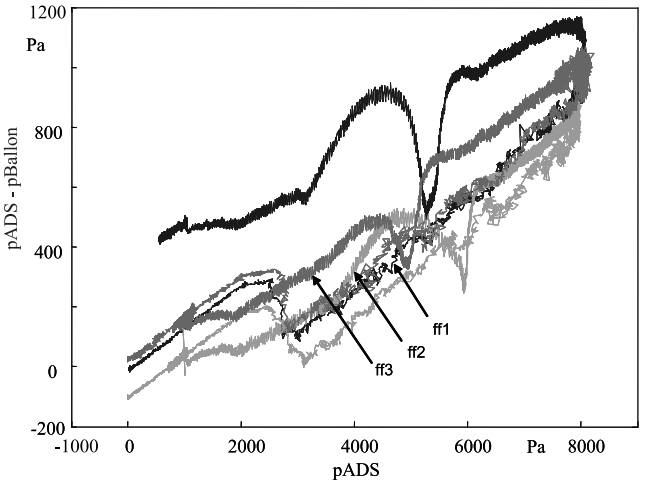

Fig. 4 Error in the measured static pressure.

$$
\begin{aligned}
CZ = {} & CZ_0(\alpha) + UD\,\mathrm{d}CZ_\alpha \cdot \alpha + DCZ_{\mathrm{EO}}(\alpha, \delta_{\mathrm{EO}}) \\
& + DCZ_{\mathrm{EI}}(\alpha, \delta_{\mathrm{EI}}) + DCZ_{\mathrm{AO}}(\alpha, |\delta_{\mathrm{AO}}|) \\
& + DCZ_{\mathrm{AI}}(\alpha, |\delta_{\mathrm{AI}}|) + DCZ_{\mathrm{RU}}(\alpha, |\delta_{\mathrm{RU}}|) \\
& + DCZ_{\mathrm{BF}}(\alpha, \delta_{\mathrm{BF}}) + UFCZ_{\mathrm{SB}} \cdot DCZ_{\mathrm{SB}}(\alpha, \delta_{\mathrm{SB}}) \\
& + [\mathrm{d}CZ_\beta(\alpha) + D\,\mathrm{d}CZ_{\mathrm{LG}}\beta(\alpha) \cdot \delta_{\mathrm{LG}}] \cdot |\beta| + DCZ_{\mathrm{LG}}(\alpha) \\
& \cdot \delta_{\mathrm{LG}} + DCZ_{\mathrm{GE}}(\alpha, \mathrm{h}_{\mathrm{AGL}}) + \mathrm{d}CZ_q(\alpha) \cdot q \cdot L_{\mathrm{ref}}/V
\end{aligned} \tag{6}
$$

where the symmetric and asymmetric deflections are given by $\delta_{\mathrm{EO}} = (\delta_{\mathrm{ERO}} + \delta_{\mathrm{ELO}})/2$, $\delta_{\mathrm{EI}} = (\delta_{\mathrm{ERI}} + \delta_{\mathrm{ELI}})/2$, $\delta_{\mathrm{AO}} = (\delta_{\mathrm{ERO}} - \delta_{\mathrm{ELO}})/2$, and $\delta_{\mathrm{AI}} = (\delta_{\mathrm{ERI}} - \delta_{\mathrm{ELI}})/2$, whereby δ_{ERO} and δ_{ELO} are the right and left outboard elevon deflections, δ_{ERI} and δ_{ELI} the right and left inboard elevon deflections, δ_R the rudder deflection, δ_{BF} the body flap deflection, δ_{SB} the speed brakes, δ_{LG} the landing gear position, h_{AGL} the altitude above ground, L_{ref} the reference length, and V the airspeed; other terms such as CZ_0, $UD\,\mathrm{d}CZ_\alpha$, DCZ_{EO}, etc. are the derivatives or aerodynamic coefficients in table forms.

D. Comparison of Wind-Tunnel and Flight-Derived Force and Moment Coefficients

Three free flights are analyzed here. The attention is restricted first to the in-air aerodynamic. To facilitate verification of landing gear effects separately, the first part of data analysis was based on 50 s long time segments corresponding to the portions starting just after the drop up to just before the landing gear is extended. The guidance maneuver in longitudinal axis results in a fair amount of pitching motion. The altitude above ground varies from 2400 to about 120 m.

Applying the procedures described in the preceding sections, aerodynamic forces and moments according to preflight ADB predictions and those from the flight measured accelerations and angular rates are computed and compared in Fig. 5. The vertical lines at 50 and 100 s demarcate the three flights. The total coefficients CX and CZ are plotted in Fig. 6 as functions of angle of attack. From Figs. 5 and 6, it is evident that there are some discernible differences between the flight-derived and wind-tunnel predicted forces and moments pertaining to the longitudinal motion. Such a comparison was not possible for (CY, CLX, CNZ), because there was no dynamic motion of the lateral-directional mode.

The rough order of magnitude of discrepancy in the vertical force coefficient (lift curve slope) was observed to be of the order of 9–10%. Briefly stated, lift generated in flight is higher than predicted and the component due to pitch rate is not adequately accounted for in the preflight ADB. The discrepancies are less than roughly 3% in the pitching-moment curve slope. Because of the nonlinear relationship, error in the axial force coefficient CX could not be quantified as in the other cases. From Figs. 5 and 6, the error in CX is evident for the clean configuration (initial portion of each segment); with increasing speedbrakes the mismatch between flight test and

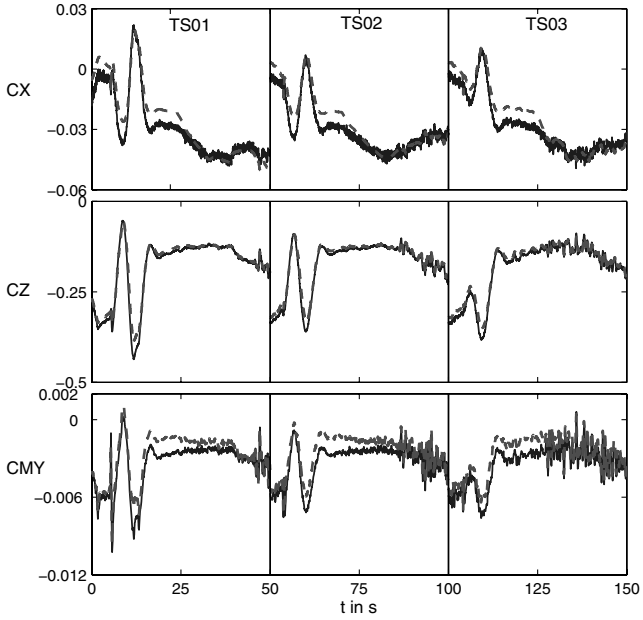

Fig. 5 Comparison of wind-tunnel predicted (solid line) and flight-derived (dashed line) aerodynamic force and moment coefficients.

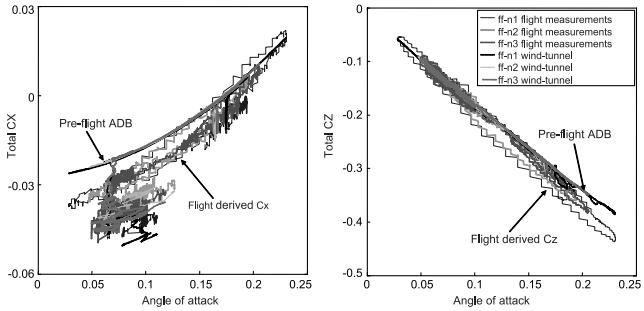

Fig. 6 Comparison of wind-tunnel predicted and flight-derived aerodynamic force and moment coefficients.

preflight database decreases, implying that the basic longitudinal force coefficient was underestimated in the wind tunnel, whereas the impact of the speedbrakes was overestimated. The preflight ADB does not account for drag due to pitch rate, which seems not to be negligible. The aerodynamic zero terms $CX0$, $CZ0$, and $CMY0$ also show deviations. The magnitudes of the deviations are typical of different test techniques [11,12]. Through a systematic approach, a better appreciation of the possible dependence of these deviations, the so-called deltas (i.e., the deviation between the flight-derived values and wind-tunnel predictions), on different motion variables was acquired. The deviations in CX were observed to be dependent on angle of attack, pitch rate, and speedbrake. The deviations in CZ were observed to be dependent on angle of attack, pitch rate, and body flap. The deviations in CMY were observed to be dependent on angle of attack and body flap.

E. Identification of Deltas for Force and Moment Coefficients

Based on the inferences drawn from the comparison, the updates for CX, CZ, and CMY are identified applying a stepwise procedure. The resulting model in terms of derivatives turned out to be as follows:

$$
\begin{aligned}
\Delta CX &= CX_0 + CX_\alpha \alpha + CX_q q/L_{\mathrm{ref}} V + CX_{\delta \mathrm{sb}} \delta_{\mathrm{sb}} \\
\Delta CZ &= CZ_0 + CZ_\alpha \alpha + CZ_q q/L_{\mathrm{ref}} V + CZ_{\delta \mathrm{bf}} \delta_{\mathrm{bf}} \\
\Delta CMY &= CM_0 + CM_\alpha \alpha + CM_{\delta e} \delta_e + CM_{\delta \mathrm{bf}} \delta_{\mathrm{bf}}
\end{aligned} \tag{7}
$$

where CZ_α and CM_α are modeled nonlinear, having one value for

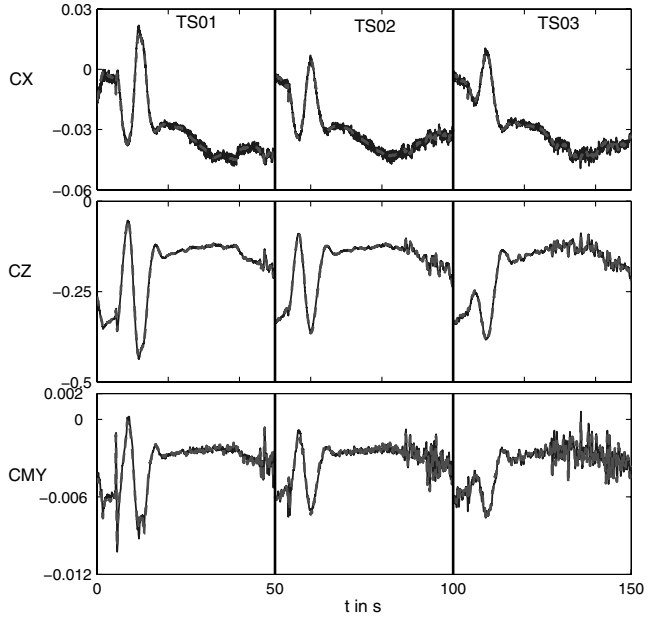

Fig. 7 Comparison of model-estimated (dashed line) and flight-derived (solid line) aerodynamic force and moment coefficients.

angle of attack up to 0.175 rad and another value for higher angle of attack. Parameters $(CX_0, CX_\alpha, CX_q, CX_{\delta\text{sb}})$, $(CZ_0, CZ_\alpha, CZ_q, CZ_{\delta\text{bf}})$, and $(CM_0, CM_\alpha, CM_{\delta e}, CM_{\delta\text{bf}})$ are estimated using the software tool FITLAB , which is a toolbox for parameter estimation under Matlab®.

The results of parameter estimation are plotted in Fig. 7 showing the force and moment coefficients [4,14]. A comparison of Figs. 5 and 7 clearly shows the improvements obtained through the updates given by the model in Eq. (7). It was observed that the residuals, i.e., the deviations between the flight-derived coefficients and those computed with updates are not any more deterministic in nature, and now represent the measurement noise. The cross plots of total coefficients CX and CZ as a function of angle of attack showed a good agreement.

It is necessary to mention here that during this phase of flight the speedbrakes and body flap are deflected simultaneously and accordingly they are correlated. As such from the available flight data it is not possible to identify the components in CX due to speedbrakes and body flap separately. The correction term is modeled with respect to speedbrake only.

Following a similar approach, the investigations were extended to analyze the portion of free flights in which the landing gear was extended. Increments were identified for the aerodynamic effects due to the landing gear.

F. Ground-Roll Characteristics

In sequel to preceding flight data analysis, it is now attempted to investigate the possibility of estimating parameters that model the tire forces and affect the ground-roll performance. A detailed description of the model for the landing gear dynamics and tire forces is not within the scope of this paper. Briefly stated, in the model for the longitudinal tire forces, the longitudinal friction coefficient for both main gear wheels is defined as

$$\mu_{x,\text{mg}} = (\delta_{\text{BR}}\mu_{\text{BR,eff}}[0.74712 - 0.00144u_K] + \mu_{\text{roll}})\frac{u_K}{|u_K|} \tag{8}$$

where δ_{BR} denotes the brake command (=0 for no braking and =1 for braking), $\mu_{\text{BR,eff}}$ the brake efficiency, μ_{roll} the rolling friction, u_K the flight-path velocity component in body-fixed frame along x-direction, and the subscript "mg" for the main gear. The brake efficiency $\mu_{\text{BR,eff}}$ varies between 0 and 1.

The nose gear is used for the steering purpose only and is not equipped with brake. Therefore, the friction coefficient for the nose gear is the same as unimpeded rolling friction μ_{roll}. Accordingly, the longitudinal friction coefficient for the nose gear is given by

$$\mu_{x,\text{ng}} = \mu_{\text{roll}}\frac{u_K}{|u_K|} \tag{9}$$

In the lateral direction, the resultant friction coefficient perpendicular to a wheel is modeled as

$$\mu_{y,i} = \mu_{y,\max,i}(\phi_i - 0.148\phi_i^3) \tag{10}$$

where the index "i" in the subscript refers to rw, lw, and nw for the right, left, and nose wheel, respectively. The maximum lateral friction coefficients $\mu_{y,\max,i}$ vary with the forward speed component u_K and the brake command δ_{BR}. The function ϕ_i appearing in Eq. (11) is given by

$$\phi_i = \min\left\{1.5, \max\left[-1.5, \mu_{y,\text{lin}}\frac{\tau_i}{\mu_{y,\max,i}}\right]\right\} \quad \text{with } i = \text{rw, lw, nw} \tag{11}$$

where τ_i are the slip angles of the right, left, and nose wheels, and $\mu_{y,\text{lin}}$ the linear dependence of the lateral friction coefficient on slip angle which is assumed same for all the three wheels.

From the model postulated in Eqs. (8–11), the three parameters that characterize the ground-roll behavior are: 1) rolling friction μ_{roll}, 2) brake efficiency $\mu_{\text{BR,eff}}$, and 3) lateral friction coefficient slip derivative $\mu_{y,\text{lin}}$. The nominal values used in the simulation studies before free flights are as follows: $\mu_{\text{roll}} = 0.043$, $\mu_{\text{BR,eff}} = 0.22$, and $\mu_{y,\text{lin}} = 4.2972(=0.075 * 180/\pi)$. From the ground-roll data recorded during the free flights with Phoenix, it is now attempted to verify the preceding three friction parameters. Accordingly, conforming to the goal of these investigations, the attention is restricted to the analysis of recorded data corresponding to the ground-roll phase only.

At the beginning, it was uncertain whether the attempts to simulate the complete model fed with the measured control deflections as inputs and simulation carried out in open-loop would be successful or not. However, it turned out that it was possible to perform such simulation, although the model is somewhat sensitive to the starting values for the initial conditions on the state variables, particularly for the tire compressions. Furthermore, reliable wind information was not available, and hence constant wind components uWG and vWG in the x- and y-directions, as well as the initial conditions (ψ_0, r_0, vK_0) were estimated. The brake efficiency $\mu_{\text{BR,eff}}$ was estimated to be 0.1917 which resulted basically from matching the travel in x-direction and the time point at which the vehicle comes to standstill. It is somewhat lower than the nominal value of 0.22. The estimation of lateral friction coefficient slip derivative $\mu_{y,\text{lin}}$ was more difficult, mainly due to lack of movement in the lateral direction during ground roll. Only during the third flight, due to unfavorable conditions, ground roll showed some lateral deviations from the centerline. Results of identification for this case are shown in Fig. 8, which show marginal match for the lateral position and true heading. These deviations are attributed to several influencing factors like turbulent atmospheric conditions. The match for the ground roll of the first free flight, which was under ideal weather conditions, showed significantly better match (not shown here). The estimation results tend to indicate slightly smaller value for the slip derivative compared to the nominal value of 4.2972. However, due to very high sensitivity of the model to extremely small deviations in any one of the influencing factors in the absence of exact wind information and due to uncertainties in the aerodynamic model valid over ground, it is considered futile to estimate such finer details of the ground-roll behavior from the flight/ground-roll data available. It is anticipated that the special ground-roll tests carried out under controlled conditions with larger excursions in the lateral directions would enable better identification of the friction coefficient slip derivative.

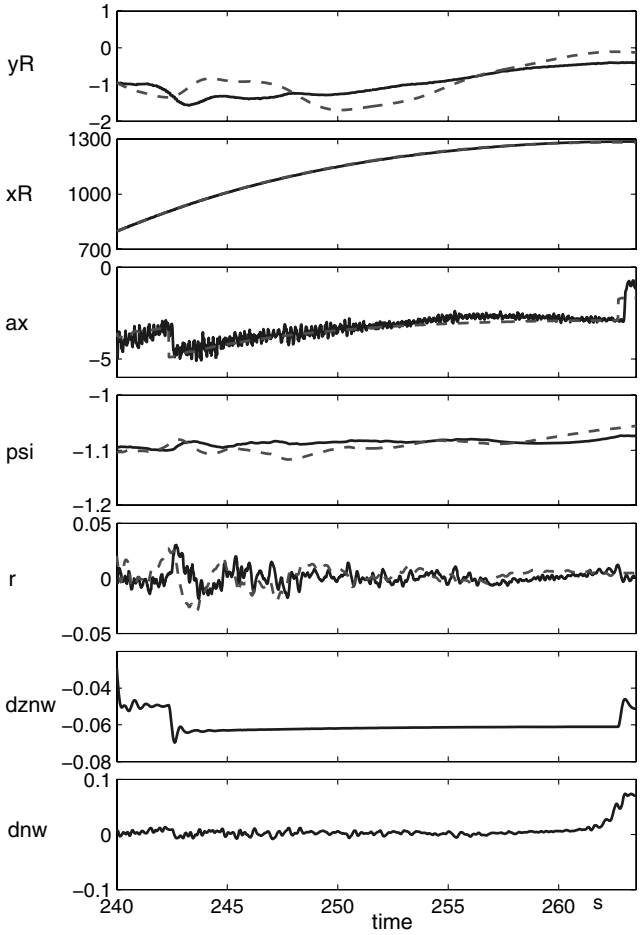

Fig. 8 Ground-roll characteristics.

V. Concluding Remarks

An elaborative account of the Phoenix project demonstrating automatic and unpowered landing of a representative winged reusable launch vehicle was presented. Detailed description of the various wind-tunnel campaigns has been provided; those were performed to arrive at the aerodynamic shape, control surface configurations, as well as predicted aerodynamic database for simulation, analysis, and design of control laws. The wind-tunnel calibration of the air-data-sensors was performed at three typical speeds and nonlinear sensitivity factors for the flow angles were estimated to meet the required accuracy requirements. Details of the highly successful flight tests have been provided, which has been an important milestone of the German ASTRA Program.

The flight recorded data from the three free flights and ground roll has been analyzed applying system identification methods. After verification of the wind-tunnel predicted aerodynamic characteristics, update for the forces and moments pertaining to the longitudinal motion were modeled and estimated. The rough orders of corrections required to the prediction were 3–10%. It was found that the lift generated in flight is higher than predicted and the component due to pitch rate is not adequately accounted for in the preflight aerodynamic database. The results from system identification emphasize that the basic longitudinal force coefficient for clean configuration was underestimated in the wind tunnel, whereas the impact of the speedbrakes was overestimated. Update of the forces and moments pertaining to the sideforce, rolling, and yawing moments was not possible, because there was no dynamic motion of the lateral-directional mode. The analysis of the landing gear system showed some discrepancies, which could not be directly interpreted as deviations in the wind-tunnel predictions because of the nonretracted door-flap configuration which was not tested in wind tunnel. The landing gear effects as modeled here are valid for the configuration tested, which may not be applicable to the future vehicles.

Analysis of ground roll in the open loop was feasible, but was sensitive to the initial conditions on the states, particularly the tire compression. The brake efficiency could be identified reasonably well, whereas the estimation of lateral friction coefficient slip derivative was not conclusive, mainly due to the lack of information in the data analyzed. The data analysis of the three free flights applying system identification has thus provided updated aerodynamic database for future studies and applications.

Acknowledgments

The Phoenix project was performed in a joint national effort of the federal state of Bremen, the German Aerospace Center (DLR), and EADS-ST as a prime contractor. Involved partners were OHB (Bremen) for the additional flight-test instrumentation and parts of the navigation system; Zarm (Bremen) for parts of the navigation and also the FTI; DLR-Institute of Flight systems to support Hardware-in-the-Loop tests, navigation and flight data analysis applying system identification techniques; DLR-MORABA for the telemetry/telecommand system as well as the parachute system, and North European Aerospace Test Range (NEAT) for test range operation and the flight-test certification. The ASTRA Program was partly funded by the DLR-German Aerospace Center, Bonn, Germany. The Phoenix 1 project was cofunded by the federal state of Bremen, Germany.

References

[1] Spiess, J., "HOPPER ein ASTRA-Systemkonzept" (in German), DGLR Paper JT2000-070, Sept. 2000.

[2] Dittmann, R., Brücker, E., and Noack, E., "ASTRA Das deutsche Technologieprojekt für zukünftige Raumtransportsysteme" (in German), DGLR Paper JT2000-117, Sept. 2000.

[3] Gockel, W., Kyr, P., Janovsky, R., and Roenneke, A., "Reusable RLV Demonstrator Vehicles—Phoenix Flight Test Results and Perspectives," IAC Paper 04-V.6.04, Oct. 2004.

[4] Jategaonkar, R. V., Behr, R., Gockel, W., and Zorn, C., "Data Analysis of Phoenix RLV Demonstrator Flight Test," AIAA Paper 2005-6129, Aug. 2005.

[5] Janicik, J. L., "The Phase 1 Space Maneuver Vehicle Test Program—Leading the United States into 21st Century Space Test and Evaluation," AIAA Paper 1999-4539, Sept. 1999.

[6] Yanagihara, M., Shigemi, M., and Suito, T., "Estimating Aerodynamic Characteristics of Automatic Landing Experiment Flight Experiment Vehicle Using Flight Data," *Journal of Aircraft*, Vol. 36, No. 6, 1999, pp. 926–933.

[7] Zorn, C., and Jategaonkar, R. V., "Calibration of Phoenix Air Data System from Wind Tunnel Tests," DLR-IB Paper 111-2003/35, Nov. 2003.

[8] Parameswaran, V., Jategaonkar, R. V., and Press, M., "Five-Hole Flow Angle Probe Calibration from Dynamic and Tower Flyby Maneuvers," *Journal of Aircraft*, Vol. 42, No. 1, 2005, pp. 80–86.

[9] Behr, R., "Phoenix: Aerodynamic Data Base, Version 3.1," EADS-ST, Rept. PHX-DP-01, No. 1, Jan. 2004.

[10] Gockel, W., "Phoenix Definition & Justification File—Plant Model," EADS-ST, Rept. PHX-DDD-008, No. 3, Jan. 2004.

[11] Kirschstein, S., and Alles, W., "Parameter Identification with a Controlled Free Flying Model of a Spaceplane," DGLR Paper JT2004-190, Sept. 2004.

[12] Cobleigh, B. R., "Development of the X-33 Aerodynamic Uncertainty Model," NASA Paper TP-1998-206544, April 1998.

[13] Seher-Weiß, S., "FITLAB, Parameter Estimation Using MATLAB," DLR-FT Report 2003, former DLR-IB Paper 111-1999/32, Dec. 1999.

[14] Zorn, C., and Jategaonkar, R. V., "Flight Path Reconstruction, Aerodynamic Model Verification and Update from Phoenix Free Flight Data," DLR-IB Paper 111-2004/46, July 2004.